

A Correct Smoothed Particle Method to Model Structure-Ice Interaction

Yang Liu^{1,*}, Yue Qiao² and Tiange Li³

Abstract: This paper studies the effect of ice resistance on the icebreaking capacity and speed of an icebreaking vessel. We combine an improved Correct Smoothed Particle Method (CSPM) with a material low-speed collision fracture model to numerically simulate the continuous icebreaking and rolling process of crushed. Using this model, we investigate the icebreaking resistance and immersion resistance during the icebreaking process, taking into account the fluid (water) as the elastic boundary support and the fluid-solid coupling interaction. We compare the icebreaking resistance and broken ice fracture shapes obtained by the numerical calculation with the theoretical analytical results, and thus validate the improved CSPM method. Further, we compare the immersion resistance results from our simulation against that from Puntigliano [Puntigliano, Hamburgische Schiffbau-Versuchsanstalt GmbH (1995)], and demonstrate that the proposed method can accurately predict ice resistance.

Keywords: SPH, ice resistance, fluid-structure interaction, numerical simulation, ventilation phenomenon.

1 Introduction

Ice resistance is an important concern for ice-going vessels. Besides, it is an important basis for host power calculations and hull design, and also has a direct impact on the icebreaking capacity and speed of a vessel. There are three main ice-resistance research methods. The first is the empirical formula for calculating resistance based on experimental data, such as the Lindqvist method [Lindqvist (1989)], Keinonen method [Keinonen and Browne (1991)], and Riska method [Riska (1997)], which are commonly used in the level ice environment. Buzuev et al. [Buzuev and Ryvlin (1961)] proposed the empirical formula for ice resistance in different ship types and ice conditions, and Kim et al. [Kim, Kim, Choi et al. (2013), Kim, Ryu, Park et al. (2014)] replaced the empirical coefficient in the empirical formula of ice resistance with the hull-type parameters. The second is the model or full-scale ship experiment method. Mueller [Mueller and Ettema (1984)] established the calculation method of the vertical ice force of the hull for the continuous icebreaking process. Kim et al. [Kim, Lee and Shin (2014)] discussed the

¹ College of Shipbuilding Engineering, Harbin Engineering University, Harbin, 150001, China.

² China Ship Research and Development Academy, Beijing, 100101, China.

³ Department of Civil and Environmental Engineering, University of California, Berkeley, CA 94720, USA

* Corresponding Author: Yang Liu. Email: qingtianriji@126.com.

influence of the ice flotation scale on the resistance by calculating the ice density. Valanto [Valanto (1989)] studied the proportion of ventilation in two-dimensional and three-dimensional cases in ice resistance. However, these methods demonstrate features such as excessive time consumption, high cost and limited test conditions. The third one is a numerical simulation method based on the ship motion equation to describe the dynamic process of the ship and ice interaction. Jebaraj et al. [Jebaraj, Swamidas and Shih (1989); Jebaraj, Swamidas, Shih et al. (1992)] studied the collision-type icebreaking process based on the finite element method (FEM). Vegard [Aksnes (2010)] proposed a calculation model of ice resistance based on elastic beam theory and friction theory. Daniela [Myland and Ehlers (2014)] explored the effects of speed, ice thickness, and ship-type parameters on ice resistance. Yamaguchi et al. [Yamaguchi, Suzuki, Uemura et al. (1997)] studied the effect of bow shape on ice resistance in low-speed icebreaking conditions. Cho et al. [Cho, Jeong and Lee (2013)] performed a series of experimental and numerical simulation studies related to ice resistance used non-refrigerated ice material. Hansen et al. [Hansen and Løset (1999)] and Karulin et al. [Karulin and Karulina (2011)] calculated the ice resistance during the ship-floating ice process and compared it with the model test. Lau et al. [Lau, Lawrence and Rothenburg (2011)] and Konno et al. [Konno, Saitoh and Watanabe (2011)] used discrete element method (DEM) software to calculate the icebreaking ability and maneuverability of a ship. Sawamura [Sawamura (2012)] proposed a three-dimensional calculation method for ice resistance including icebreaking resistance and immersion resistance.

Despite the development of some important concepts nowadays, it is still a big challenge of classical continuum mechanics to predict crack initial condition and growth within the framework in the area of materials and structures. The mathematical formulation that assumes a body keeps continuous during deformation is the main difficulty. However, when the discontinuity appears, the basic assumption fails. Spatial partial differential equations are used by the classical theory. In the theory, the spatial derivatives are not defined at discontinuities, which is an inherent limitation. The spatial derivatives, by definition, lose their meaning in governing equations once discontinuity appear, such as a crack [Madenci and Oterkus (2014)].

The meshless method has significant advantages in the calculation of discontinuous problems because of its discrete characteristics, and has been gradually applied to the numerical analysis of ice mechanics [Li and Liu (2002)]. Liu et al. [Liu, Xue, Lu et al. (2018)] used the peridynamics method to study ships' ice resistance in ice rubble and analyzed the ice resistance with respect to different factors; however, the ice material is overly simplified. The smoothed particle hydrodynamics (SPH) proposed by Gingold et al. [Gingold and Monaghan (1977) and Lucy [Lucy (1977)]] is a Lagrangian meshless method, which is not bounded by the grid and can effectively display and track the physical quantities of each material point. Further, it is easy to embed multiple material models, which offers clear advantages in solving multi-medium coupling problems. In recent years, this method has been widely applied to address structural dynamics problems, mainly for structural large deformation disintegration, fragmentation, and other analysis (such as high-speed collision and fluid-structure coupled). Such as the shear and tensile failure of a rock specimen under uniaxial loading conditions [Deb and Pramanik (2013)], the brittle fracture behavior of plates considering plastic response under the

water impact [Eghtesad, Shafiei and Mahzoon (2012)], the fluid-structure interactions [Khayyer, Gotoh, Falahaty et al. (2018); He, Bayly and Hassanpour (2018)], and the failure process of a flexible oil boom enduring the waves and currents [Shi, Li, Chen et al. (2018)]. In addition, with the strength of Lagrangian method, SPH shows an effective way to simulate the large deformation and failure behavior of solid [Libersky and Petschek (1991); Benz and Asphaug (1995); Randles and Libersky (1996); Bui, Fukagawa, Sako et al. (2008); Deb and Pramanik (2013); Zhang, Zheng and Ma (2017)]. For more details see [Liu and Liu (2010); Liu (2016)]. However, the icebreaking process is a complex problem where the influence of velocity is relatively high and includes multi-media coupling. In the traditional SPH method, especially when the particle distribution is not uniform or the boundary conditions are complicated, the accuracy of the function value and its derivative value after the kernel approximation can deteriorate, and there are serious numerical dissipation problems. Then, the subsequent particle approximations convert successive integral forms into discrete forms and create new errors.

To improve the computational accuracy of SPH in solving solid mechanics problems, Chen [Chen (2010)] proposed the CSPM, which improved the accuracy of numerical simulation. Based on this, considering the density correction, artificial stress correction, and speed correction, the improved CSPM method is combined with the material low-speed collision fracture model. Considering the fluid as the elastic boundary support and the fluid-solid coupling interaction, the icebreaking resistance and immersion resistance during the icebreaking process, respectively, are investigated. The ice resistance obtained by numerical simulation is compared with the analytical solution and experimental results, and the accuracy of the icebreaking resistance and immersion resistance is verified.

The paper is organized as follows: The simplified icebreaking theoretical solution is given in Section 2. In Section 3, the basic formulations of CSPM is reviewed. In Section 4, the validations and convergence are conducted. The simulations of ice-structure are presented in Section 5 comparing the coupling model and Immersion resistance is predicted in Section 6. We conclude the work in the last section with some discussions.

2 Ice-resistance distribution and icebreaking mechanism

In the process of interaction between slope structure and level ice, the interaction is different in different interaction stages, and it can be divided into the icebreaking stage, rotational slip stage, final stage and propeller action stage. Considering the ship bow as an example, in the process of continuous icebreaking, the total ice resistance at the bow includes icebreaking resistance and immersion resistance. Ice resistance at the icebreaking stage and rotational slip stage are distributed at the waterline. The proportion of ice resistance at the slip stage is smaller. The immersion resistance arises, beginning from the waterline, downward the length of the ice block under the water. Following this, only ice slipping resistance remains while the other disappears (Fig. 1).

Based on the characteristics of resistance distribution in different hull areas at different stages, the components of ice resistance are measured by the method of dividing the model into blocks according to the model tests [Liukkonen and Nortala-Hoikkanen (1992); Kayo (1993)]. In the process of numerical simulation, the components of ice resistance are also extracted according to the different structure-ice interaction regions.

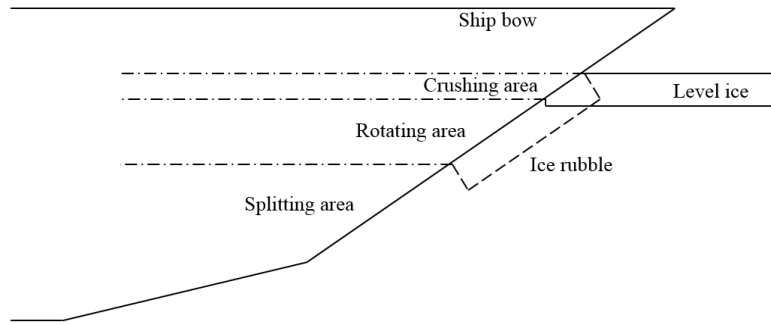


Figure 1: Characteristics of ice-resistance distribution on bow

For structures with inclined angles, the failure is determined mainly by tensile and bending rather than compression. Therefore, this paper uses a slope as a simplified model to theoretically analyze the process of icebreaking. Assuming that the ice thickness is h , the slope structure is at constant speed v , as indicated in Fig. 2. In the process of interaction, the free end of the level ice is subjected to a concentrated load, which can be decomposed into vertical and horizontal loads in each time step, and increases with the increase of the contact area between the structure and ice. When the load reaches the bending strength, the level ice breaks. The distance from the fracture to the contact point is the fracture length.

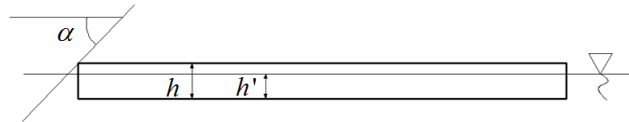


Figure 2: Interaction between ice sheet and structure

The forces acting on the level ice, as illustrated in Fig. 3, can be decomposed into F_h and F_v ,

$$F_h = \sin \alpha F_n + \mu \cos \alpha F_n \tag{1}$$

$$F_v = \cos \alpha F_n - \mu \sin \alpha F_n \tag{2}$$

where F_h and F_v are the forces in the horizontal and vertical directions, respectively. F_n is the force in the normal direction.

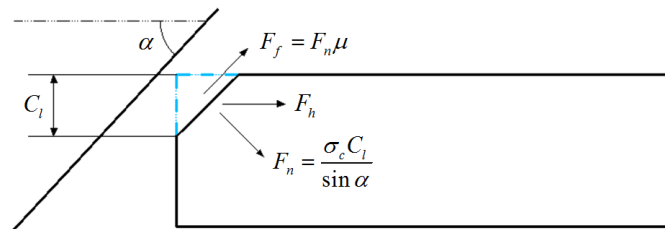


Figure 3: Mechanical analysis between ice sheet and structure

The level ice can be simplified as a beam structure acting on an elastic foundation; the equilibrium equation of the beam is

$$EI \frac{d^4 w}{dx^4} + kw = 0 \quad (3)$$

where E is the elastic modulus of ice, I is the moment of inertia of the beam, k is the stiffness of elastic support, and w is the deflection of the beam.

The maximum bending moment and maximum shear force are

$$M_{\max} \Big|_{x=\frac{\pi}{4}l} = -F_v \sqrt{2} L_b \sin \frac{\pi}{4} e^{-\frac{\pi}{4}} \quad (4)$$

$$T_{y \max} \Big|_{x=\frac{\pi}{4}l} = \frac{6\sqrt{2} F_v L_b}{bh^2} \sin \frac{\pi}{4} e^{-\frac{\pi}{4}} \quad (5)$$

The vertical force acting on the ice sheet is

$$F_v = \frac{\sigma_f bh^2}{6\sqrt{2} L_b \sin \frac{\pi}{4}} e^{\frac{\pi}{4}} \quad (6)$$

The maximum breaking length of the crushed ice is

$$L_{B, \max} = \frac{\sqrt{2}\pi}{4} \left(\frac{EI}{k} \right)^{\frac{1}{4}} \quad (7)$$

3 CSPM fundamental basis

The SPH method was first proposed in 1977 by Gingold et al. [Gingold and Monaghan (1977)] and Lucy [Lucy (1977)]. It was used to solve astrophysics problems. The basic idea is to express the problem domain with arbitrarily distributed particles carrying physical quantities such as density, pressure, velocity, and internal energy. By solving the governing equations, the trajectory of each particle and the change of physical quantities, and then, the mechanical behavior of the entire system can be obtained. The principle of the SPH method is to interpolate and approximate the variables of the particles through a kernel function in the computational domain. This makes the SPH method meshless, adaptive, stable and Lagrangian. In recent years, this method has been gradually employed to solve problems related to ice mechanics. The solution process transfers the differential equation into an integral equation using a kernel approximation method, and then further approximates the kernel approximation equation using a particle approximation method. The integral expression is transformed into the superposition sum of all the particles in the support domain [Monaghan (1994); Li and Liu (2002); Liu and Liu (2003)].

The kernel approximation and particle approximation can be expressed as

$$f(x) = \int_{\Omega} f(x') \delta(x - x') dx' \quad (8)$$

$$f(x) = \sum_{j=1}^N \frac{m_j}{\rho_j} f(x_j) W_{ij} \quad (9)$$

$$\nabla f(x) = \sum_{j=1}^N \frac{m_j}{\rho_j} f(x_j) \nabla_i W_{ij} \quad (10)$$

The selection of a kernel function determines the approximation accuracy and computational efficiency; it also reflects the degree of interaction between the particles. When the distance between the particles increases, the degree of interaction decreases. In this paper, we use the quantic spline kernel function,

$$W(R, h) = \alpha_d \times \begin{cases} (3-R)^5 - 6(2-R)^5 + 15(1-R)^5, & 0 \leq R < 1 \\ (3-R)^5 - 6(2-R)^5 & , 1 \leq R < 2 \\ (3-R)^5 & , 2 \leq R \leq 3 \\ 0 & , else \end{cases} \quad (11)$$

where $R = r_{ij} / h$, r_{ij} is the distance between particle i and particle j , and h is the smooth length. For plane stress, $\alpha_d = 7 / (478\pi h^2)$.

Using the particle approximation, the governing equations in the form of SPH can be expressed as

$$\begin{cases} \frac{d\rho_i}{dt} = \sum_j m_j \frac{\rho_i}{\rho_j} (\mathbf{v}_i^\beta - \mathbf{v}_j^\beta) W_{ij,\beta} \\ \frac{d\mathbf{v}_i^\alpha}{dt} = \sum_{j=1}^N m_j \left(\frac{\sigma_i^{\alpha\beta}}{\rho_i^2} + \frac{\sigma_j^{\alpha\beta}}{\rho_j^2} + \Pi_{ij} \delta^{\alpha\beta} + R_{ij}^{\alpha\beta} f_{ij}^n \right) \nabla_i W_{ij} \\ \frac{d\mathbf{e}_i}{dt} = -\frac{1}{2} \sum_j m_j (\mathbf{v}_i^\alpha - \mathbf{v}_j^\alpha) \left(\frac{\sigma_i^{\alpha\beta}}{\rho_i^2} + \frac{\sigma_j^{\alpha\beta}}{\rho_j^2} - \Pi_{ij} \delta^{\alpha\beta} \right) W_{ij,\beta} \end{cases} \quad (12)$$

where Π_{ij} is the Monaghan artificial viscosity [Monaghan (1994)] and $R_{ij}^{\alpha\beta}$ and f_{ij}^n are artificial stress items defined as

$$\begin{aligned} R_{ij}^{\alpha\beta} &= R_i^{\alpha\beta} + R_j^{\alpha\beta}; \\ R_i^{\alpha\beta} &= \begin{cases} -\varepsilon_r \sigma_i^{\alpha\beta} / \rho_i^2 & (\sigma_i^{\alpha\beta} > 0), \\ 0 & (\text{other}); \end{cases} \\ f_{ij}^n &= W(r_{ij}) / W(\Delta p), \end{aligned} \quad (13)$$

where $n = 2.55$, $\varepsilon_r = 0.5$, and Δp is the initial distance between particles.

Π_{ij} is defined as

$$\Pi_{ij} = \begin{cases} (-\alpha_\Pi \bar{c}_{ij} \phi_{ij} + \beta_\Pi \phi_{ij}^2) / \bar{\rho}_{ij} & (\mathbf{v}_{ij} \cdot \mathbf{x}_{ij} < 0); \\ 0 & (\text{other}), \end{cases} \quad (14)$$

where c is the sound velocity, α_{Π} and β_{Π} are empirical coefficients, $\overline{c_{ij}} = (c_i + c_j) / 2$, $\overline{\rho_{ij}} = (\rho_i + \rho_j) / 2$, $\varphi_{ij} = h_{ij} v_{ij} x_{ij} / (|x_{ij}|^2 + \phi^2)$, $h_{ij} = (h_i + h_j) / 2$, $x_{ij} = x_i - x_j$, $v_{ij} = v_i - v_j$, and $\phi = 0.1h_{ij}$.

When the SPH method is introduced into the solution of solid mechanics problems, two technical difficulties are encountered. The first is how to set the boundary conditions; the second is how to overcome the problem of tensile instability. Tensile instability is the accumulation of particles of non-physical phenomena generated in the stretched state. This phenomenon is particularly noticeable in problems such as damage, fracture and debris generated in the transient tensile stress region. For traditional SPH methods, especially when the particles are not uniformly distributed or the boundary conditions are complex, the function values of the kernel approximation and the accuracy of its derivative values are deteriorated, and there are serious numerical dissipation problems. Subsequent particle approximations convert successive integral forms into discrete forms, which also creates new errors. Therefore, when the traditional SPH method is used to simulate the ice fracture, the calculation results of the fracture are unstable.

To improve the accuracy of SPH in solving solid mechanics problems, Chen [Chen (2010)] proposed a new method called CSPM. Based on the Taylor series expansion, the method performs regularization processing on the kernel approximation and particle approximation processes of the SPH method to improve the calculation accuracy.

For two-dimensional problems, the Taylor series expansion of any function $f(x,y)$ at the point (x_i,y_i) is calculated as

$$f(x,y) = f_i + (x-x_i)f_{i,x} + (y-y_i)f_{i,y} + \frac{(x-x_i)^2}{2!}f_{i,xx} + 2\frac{(x-x_i)(y-y_i)}{2!}f_{i,xy} + \frac{(y-y_i)^2}{2!}f_{i,yy} + \dots \tag{15}$$

where $f_i = f(x,y)$, $f_{i,x} = \partial f_i / \partial x$, $f_{i,y} = \partial f_i / \partial y$, $f_{i,xx} = \partial^2 f_i / \partial x^2$, $f_{i,xy} = \partial^2 f_i / \partial x \partial y$, and $f_{i,yy} = \partial^2 f_i / \partial y^2$.

Multiplying the kernel function on both sides of Eq. (14) and integrating over the entire integration domain Ω gives

$$\int_{\Omega} f(x,y)W_i ds = f_i \int_{\Omega} W_i ds + f_{i,x} \int_{\Omega} (x-x_i)W_i ds + f_{i,y} \int_{\Omega} (y-y_i)W_i ds + O(h^2) \tag{16}$$

Because the kernel function is an even function at points i , i.e., $\int_{\Omega} (x-x_i)W_i ds = \int_{\Omega} (y-y_i)W_i ds = 0$, then,

$$f_i = \frac{\int_{\Omega} f(x,y)W_i ds}{\int_{\Omega} W_i ds} + O(h^2) \tag{17}$$

For Eq. (15), replacing $\int_{\Omega} W_i ds$ with $\int_{\Omega} W_{i,x} ds$ and $\int_{\Omega} W_{i,y} ds$ obtains

$$\begin{cases} \int_{\Omega} (f(x, y) - f_i) W_{i,x} ds = f_{i,x} \int_{\Omega} (x - x_i) W_{i,x} ds + f_{i,y} \int_{\Omega} (y - y_i) W_{i,x} ds + O(h^2) \\ \int_{\Omega} (f(x, y) - f_i) W_{i,y} ds = f_{i,x} \int_{\Omega} (x - x_i) W_{i,y} ds + f_{i,y} \int_{\Omega} (y - y_i) W_{i,y} ds + O(h^2) \end{cases} \quad (18)$$

This can be rewritten as

$$f_{i,x} = \frac{\begin{vmatrix} \int_{\Omega} (f(x, y) - f_i) W_{i,x} ds & \int_{\Omega} (y - y_i) W_{i,x} ds \\ \int_{\Omega} (f(x, y) - f_i) W_{i,y} ds & \int_{\Omega} (y - y_i) W_{i,y} ds \end{vmatrix}}{\begin{vmatrix} \int_{\Omega} (x - x_i) W_{i,x} ds & \int_{\Omega} (y - y_i) W_{i,x} ds \\ \int_{\Omega} (x - x_i) W_{i,y} ds & \int_{\Omega} (y - y_i) W_{i,y} ds \end{vmatrix}} + O(h^2) \quad (19)$$

$$f_{i,y} = \frac{\begin{vmatrix} \int_{\Omega} (x - x_i) W_{i,x} ds & \int_{\Omega} (f(x, y) - f_i) W_{i,x} ds \\ \int_{\Omega} (x - x_i) W_{i,y} ds & \int_{\Omega} (f(x, y) - f_i) W_{i,y} ds \end{vmatrix}}{\begin{vmatrix} \int_{\Omega} (x - x_i) W_{i,x} ds & \int_{\Omega} (y - y_i) W_{i,x} ds \\ \int_{\Omega} (x - x_i) W_{i,y} ds & \int_{\Omega} (y - y_i) W_{i,y} ds \end{vmatrix}} + O(h^2) \quad (20)$$

4 Validations and convergence

In this section, the three-point bending model for fresh water is simulated. And numerical convergence studies of the proposed numerical method are conducted in the following examples.

A three-point bending model test is shown in Fig. 4, in which the size of the specimen is $650 \times 70 \times 70$ mm. L is the length of the specimen; L_0 is the length between two supports; b is the width of the ice beam; h is the height of the ice beam. The loading indenter moves at a constant velocity 0.763 mm/s. In accordance with the mechanical characteristics of a simply supported beam, the loading force is denoted by p , which is determined by the maximum normal stress,

$$\sigma = \frac{3pL_0}{2bh^2} \quad (21)$$

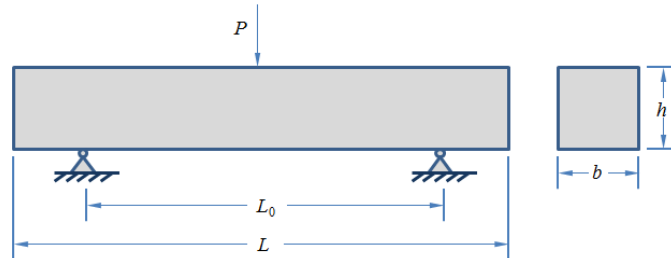


Figure 4: Schematic illustration of three-point bending model

In this section, the material is set as fresh water ice, with density of 896.977 kg/m^3 , Young modulus of 6.81 GPa , and Poisson’s ratio of 0.33 , and the compressional critical value and the tension critical value are set as 4 Mpa and 2.4 Mpa , respectively. Drucker-Prager yield criterion is used in this model. To conduct the influence of size of particle, the ice beam is discretized into $93 \times 10 \times 10$, $140 \times 15 \times 15$ and $186 \times 20 \times 20$ material points, respectively, denoted as SPH1, SPH2 and SPH3.

The numerical simulation results and experimental results are shown in Fig. 5, which shows the load-time plot for this simulation. It is observed that once the damage commences, the load carrying capacity of the beam drops very sharply to zero, indicating an elastic brittle damage type of response. The simulation results of different particle sizes show the similar trend, and the critical strength decreases as the number of particles decreases. The flexural strength can be determined from the maximal normal stress, as shown in Fig. 5. The critical strengths are 2.39 , 2.41 and 2.42 Mpa compared with 2.50 Mpa obtained from experimental data. And the errors are 4.4% , 3.6% and 3.2% , respectively. It can also be seen that with the decrease of the number of particles, the S-type fluctuation of the results tends to be gentle.

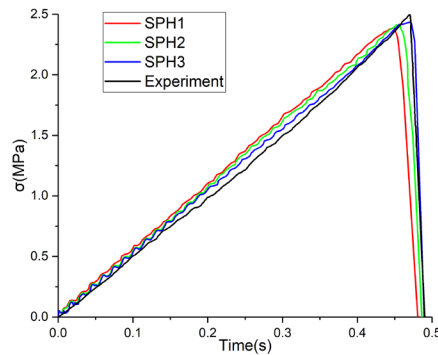


Figure 5: Critical strengths are obtained by SPH and experiment

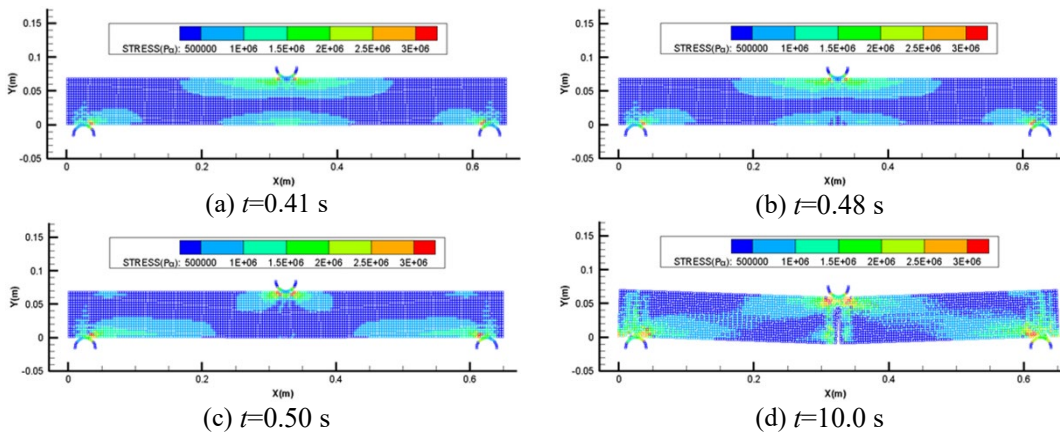


Figure 6: Contours of stress during the loading process

Fig. 6 shows the stress fields obtained by the proposed numerical method. These results show that when the loading indenter contacts the beam with a non-zero velocity, particles closest to the given indenter are the most strained. As shown in the figure, damage occurs around that region mostly, as the red particles. Failure occurs between particles, which could be seen as failure between the inter particle connections.

Fig. 7 shows the spatial distribution condition of the damage variable. Damage initially takes place at the same time with the development of the tensile damage. The contour plot in the figure also shows that the compression zone is the first damage zone. This is because that stress concentration is brought in by the transverse load, which locates at the top surface of the area near the mid-plane beam. Thus, damage is triggered in the compressive stress region.

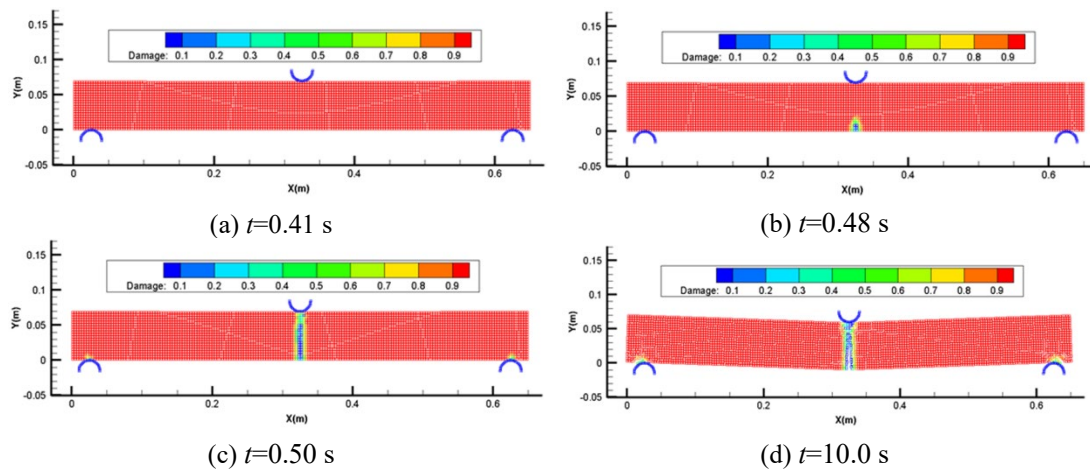


Figure 7: Contours of damage during the loading process

5 Calculation of ice resistance based on CSPM

5.1 Simulation of icebreaking stage in elastic boundary support

5.1.1 Elastic boundary support

In the icebreaking process, it is assumed that buoyancy only limits the vertical movement of the ice and that the buoyancy is proportional with the displacement of the ice.

In the rotation stage, ventilation occurs competing with the fluid backfill. If the collision speed between the slope structure and level ice is low, fluid backfilling occurs. Otherwise, the crushed ice rotates faster, the water flow is filling the gap between the crushed ice, and the ventilation phenomenon becomes apparent. Therefore, when the ice rubble is not completely submerged, the fluid below the ice can be considered as an elastic foundation. With the different ratios of the ventilation phenomenon and fluid backfilling, the repulsive force of the elastic boundary is also different. Using the spring model to represent the liquid boundary, the buoyancy per unit area of the ice can be expressed as

$$f_w = kw = \begin{cases} \rho_i gh_i & w > \frac{\rho_{ice}}{\rho_w} h_i \\ \rho_w gw & -(1 - \frac{\rho_i}{\rho_w})h_i < w \leq \frac{\rho_i}{\rho_w} h_i \\ (\rho_w - \rho_i)h_i \cdot g & w \leq -(1 - \frac{\rho_i}{\rho_w})h_i \end{cases} \quad (22)$$

where h_i is the thickness of the level ice, and ρ_i and ρ_w are the density of the ice and water, respectively.

The ventilation phenomenon and fluid backfilling effect are illustrated Fig. 8. δ is the depth of particle immersion water. It is assumed that the fluid above the ice rubble is static, and a parameter a_v is added in the elastic boundary repulsive force model to embody the ventilation.

$$f_{w,max} = \begin{cases} (\rho_w - \rho_i)hg & a_v = 0 \\ a_v \rho_w g \delta + (\rho_w - \rho_i)hg & 0 < a_v < 1 \\ \rho_w g \delta + (\rho_w - \rho_i)hg & a_v = 1 \end{cases} \quad (23)$$

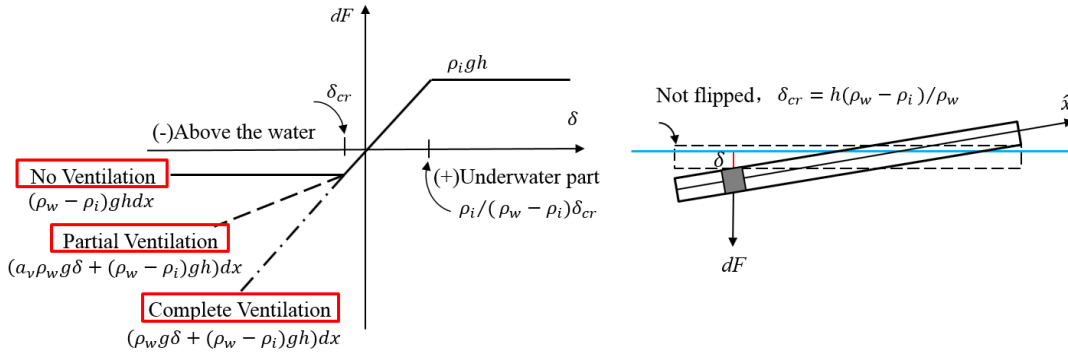


Figure 8: Buoyancy setting rule based on ventilation phenomenon

If $a_v = 1$, only ventilation occurs; there is no fluid on the upper surface of the ice rubble and the complete ventilation phenomenon is particularly evident during the icebreaking process [Valanto, Jones, Enkvist et al. (2001)]. In this situation, the relative speed of the ice and the slope structure are greater ($v \geq 0.8$ m/s). If $0 < a_v < 1$, the ventilation phenomenon and fluid backfilling both occur. If $a_v = 0$, only the fluid backfilling occurs, and the maximum repulsive force provided by the elastic boundary is constant.

5.1.2 Calculation case

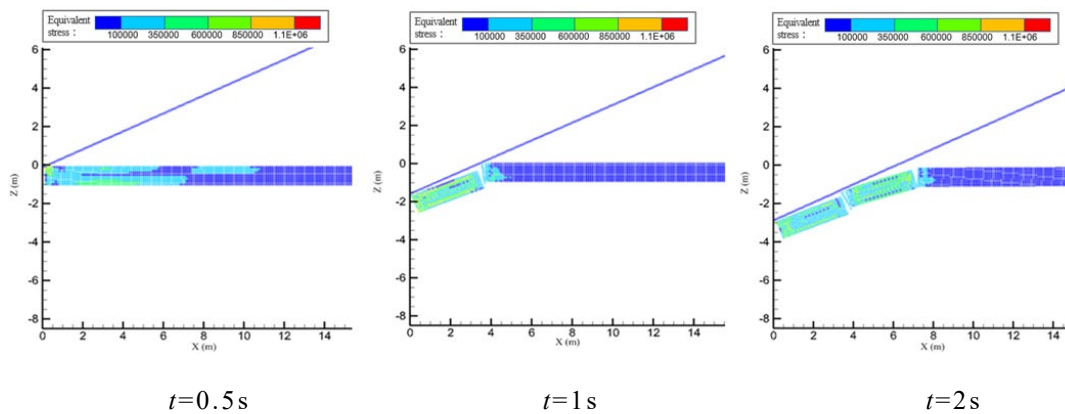
In this section, the slope has an oblique angle of 25° . The level ice, with a length of 100 m and a thickness of 1 m, is discrete uniformly by 10000 particles, among which 1000 particles in the horizontal direction and 10 particles in the vertical direction. The region

where the level ice is 10 m away from the fixed end is the damping zone, and the non-reflective boundary condition is set in this area. The slope structure moves at a constant speed of 3 m/s. $a_v = 1$ and the remaining parameters are displayed in Tab. 1. In this calculation condition, the maximum vertical force at the contact between the slope and the level ice is 103 N, and the maximum fracture length of ice rubble is 3.93 m.

Table 1: Determination of ice material parameters and numerical simulation parameters

Parameter	Symbol	Value
Slope angle	ϕ	25°
Speed of slope	v	3 m/s
Thickness of ice	h_i	1 m
Elastic module	E	4 GPa
Passion's ratio	γ	0.3
Density of ice	ρ_i	917 kg/m ³
Density of water	ρ_w	1025 kg/m ³
Artificial viscosity parameter 1	α_{II}	5.0
Artificial viscosity parameter 2	β_{II}	5.0
CSPM parameter	ε	20
Artificial stress parameter 1	ε_r	0.5
Artificial stress parameter 2	n	2.55
Smooth length	h	$1.2dx$

Fig. 9 displays the distribution of equivalent stress in the ice sheet at different times during continuous icebreaking. It can be observed that the stress is first generated in the contact area between the inclined structure and ice sheet, then transmitted to the fixed end. Because the ice sheet failure mechanism is bending failure, the upper surface of the ice sheet is first destroyed, afterwards the downward surface is broken. The broken ice rubble slides backwards along the surface of the structure. However, the combination of ice rubble and the structure is not good, mainly because the acceleration of the water flow in the gap between the ice rubble components is ignored.



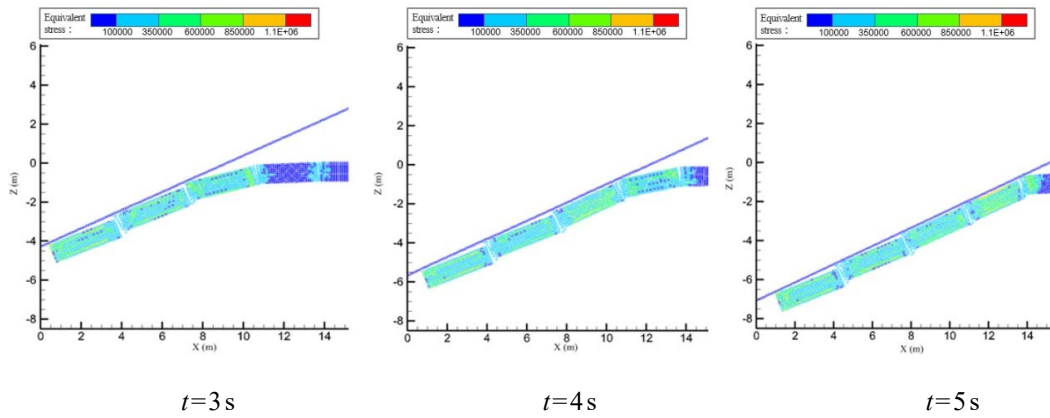


Figure 9: Contours of equivalent stress in different times

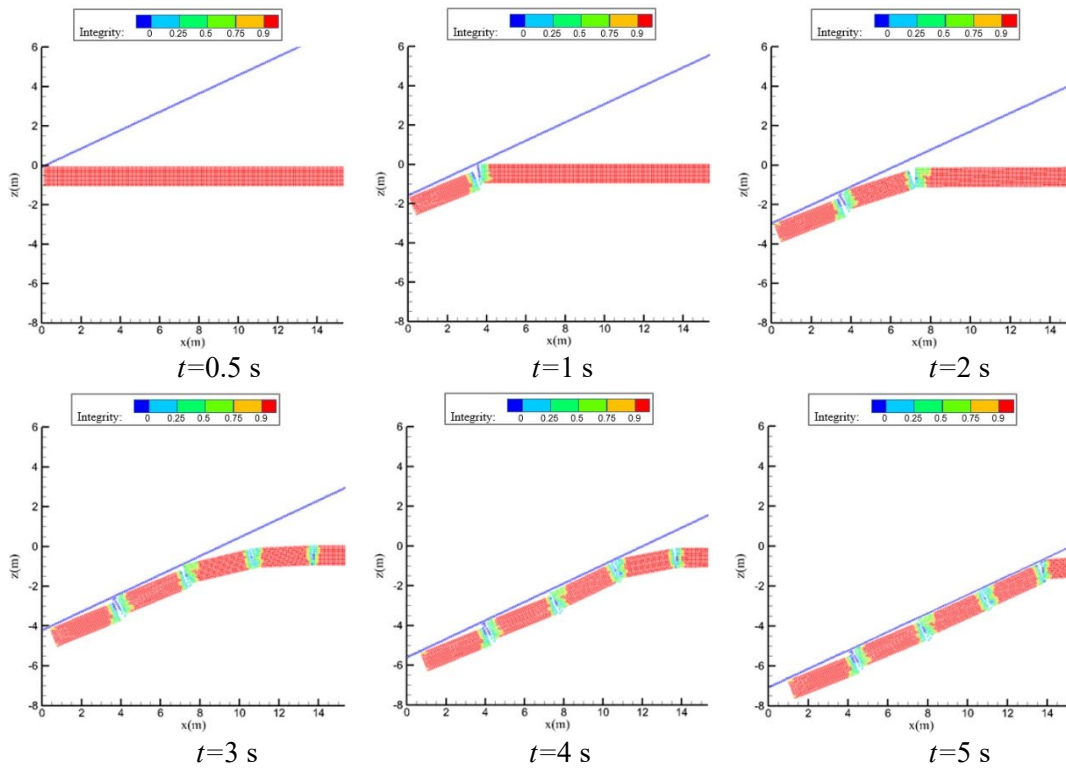


Figure 10: Contours of the integrity of ice in different times

Fig. 10 displays the completeness of the ice rubble at different times during continuous icebreaking. It can be observed that the ice rubble indicates different degrees of damage in the fracture region. The scale of each ice rubble component is consistent with the analytic solution; they are 3.90 m and 3.93 m, respectively.

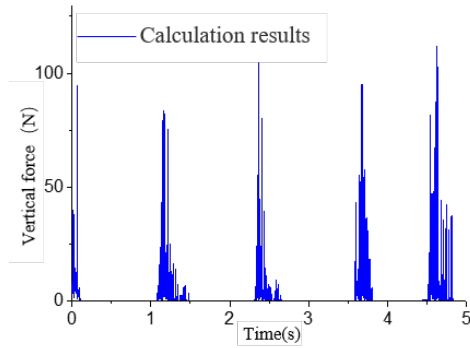


Figure 11: Vertical-force versus time

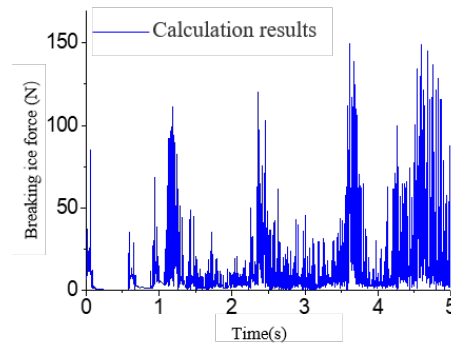


Figure 12: Breaking ice-resistance versus time

Fig. 11 and Fig. 12 display the vertical-force time curve between the structure and ice sheet (excluding the sliding process of the ice rubble) and the resultant force-time curve during the icebreaking process. It can be observed that as the ice sheet is destroyed periodically, the vertical force of the structure also demonstrates periodicity. When the ice sheet is destroyed, the ice rubble rotates and slides along the surface of the structure, and the force is significantly less than that in the process of conduct. During the ice sheet-destruction stage, as time elapses, the amount of ice rubble gradually increases, and the force acting on the slope caused by the rotation and slip of the ice rubble gradually increases.

5.2 Simulation of icebreaking in fluid-solid coupling

5.2.1 Fluid-solid coupling boundary condition

In the process of icebreaking, the fluid's effect can be simplified and to be seen as the elastic base boundary conditions, and also can be considered as SPH particles. A fluid-solid coupling model can be established according to the kinetic equilibrium and kinematic equilibrium conditions. In this section, the junction between the solid and fluid follows the Lennard-Jones repulsion model to generate an external repulsion alignment of the particles; the physical quantities of the fluid particles continue to be updated following the conservation of mass and the law of conservation of momentum,

$$\begin{cases} \frac{d\rho_i}{dt} = \sum_{j=1}^N m_j (v_i - v_j) \cdot \nabla_i W_{ij} \\ \frac{dv_i}{dt} = -\sum_{j=1}^N m_j \left(\frac{p_i}{\rho_i^2} + \frac{p_j}{\rho_j^2} \right) \nabla_i W_{ij} + F \end{cases} \quad (24)$$

where F is the external repulsion force and P is the pressure of the fluid particle.

Monaghan [Monaghan (1994)] simulated the equation of state of free surface flow; the expression is

$$p = B \left[\left(\frac{\rho}{\rho_0} \right)^\gamma - 1 \right] \quad (25)$$

$$B = 100gd\rho_w / \gamma \tag{26}$$

where γ is the calculation parameter and is set as 7, d is the depth of water.

5.2.2 Calculation case

Fig. 13 displays the distribution of equivalent stress in the ice sheet at different times during the continuous icebreaking process for 5 s. It can be observed that the stress is generated by the contact area and then transmitted to a distant location. The bending damage of the ice sheet starts from the upper surface of the ice sheet and then spreads to the lower surface of the ice sheet. The water fills the gap between the ice rubble components.

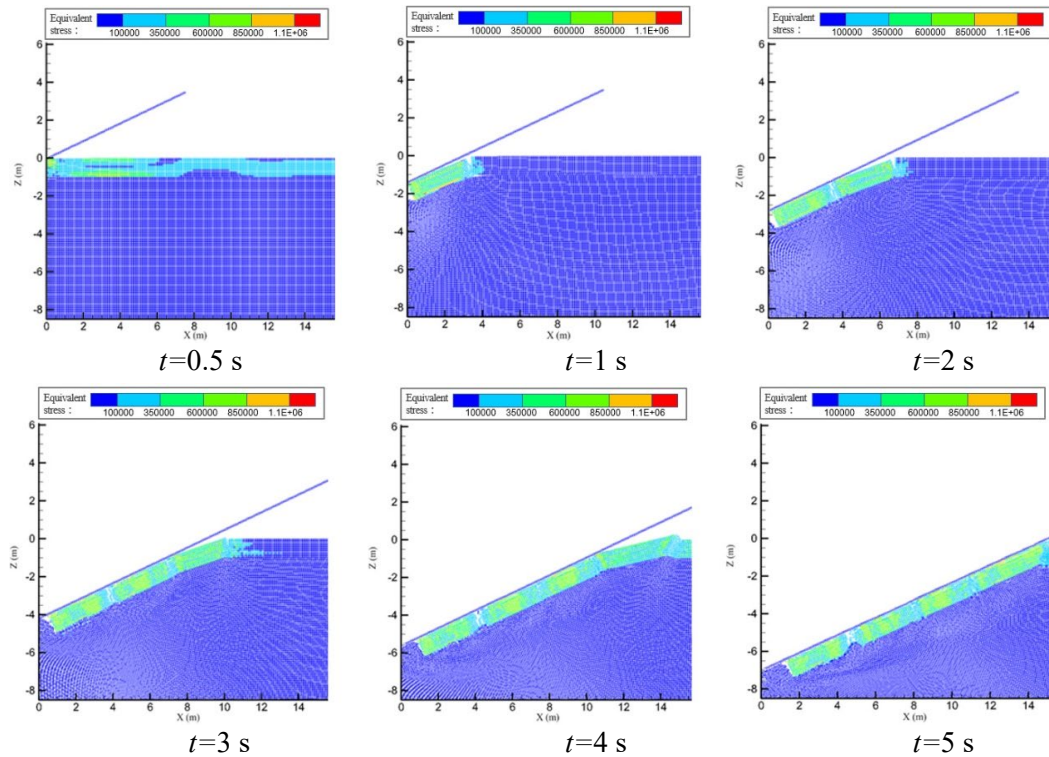


Figure 13: Contours of equivalent stress in different times

Fig. 14 displays the integrity of the ice at different times during the continuous icebreaking process. It can be observed that the length of the crushed ice is marginally greater than the value of the analytical solution, which are 3.95 m and 3.93 m, respectively. The reason is that the interaction between the water particles and ice particles is reflected by the repulsive force between these particles, which is different from the spring stiffness value set in the analytical solution.

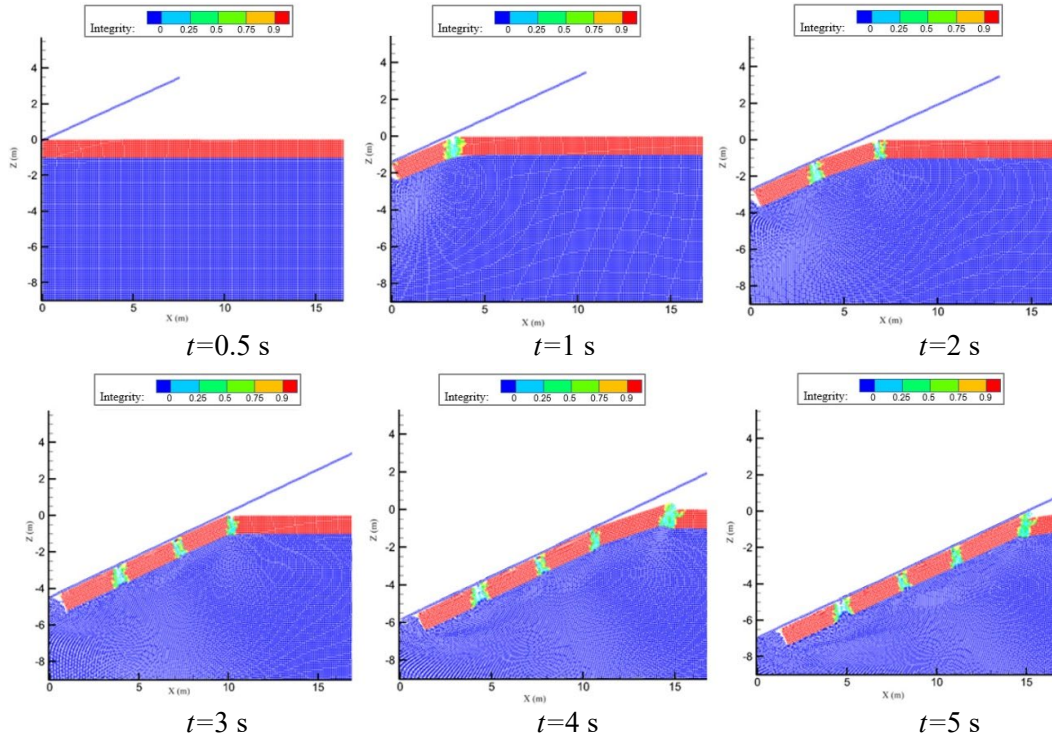


Figure 14: Contours of damage in different times

Fig. 15 and Fig. 16 display the force time curve in the vertical direction between the structure and ice sheet and resultant force time curve during the 5 s continuous icebreaking process (excluding the sliding process of the crushed ice). It can be observed that the characteristics of the vertical-force time curve conform to the process of contact-bending fracture-slipping, and that the peak of ice resistance at each stage matches that in the icebreaking process and that of the ice rubble rotation and slipping process.

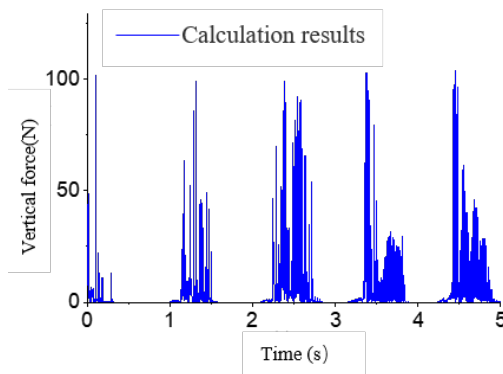


Figure 15: Vertical-force history curve

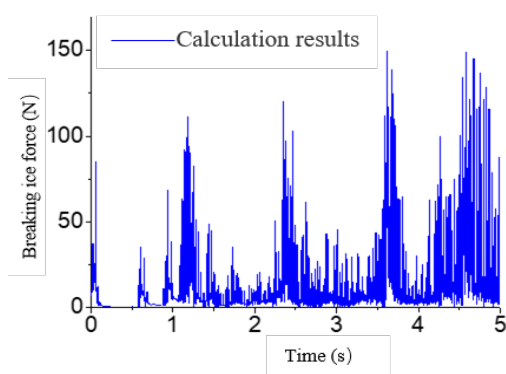


Figure 16: Breaking ice-force history curve

6 Immersion resistance prediction based on improved CSPM

For the submerged resistance, the test by Puntigliano [Puntigliano, Hamburgische Schiffbau-Versuchsanstalt GmbH (1995)] was numerically simulated using the improved CSPM method, and the calculated value of the ice resistance of the structure in the rotary slide of the crushed ice is obtained; the calculated value of immersion resistance is validated against the test results. The fluid boundary is set as the elastic base boundary and real fluid boundary, and the boundary conditions were the same as Sections 5.1.1 and 5.2.1, respectively.

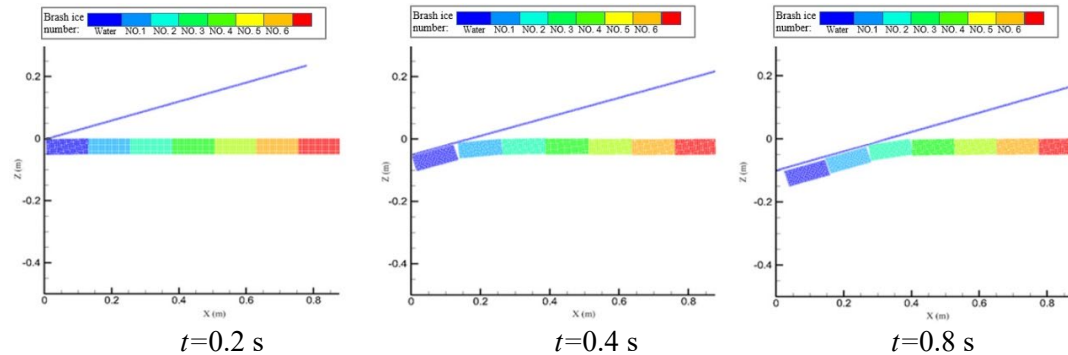
In this study, the ship bow is divided into two zones, Segment 1 and Segment 2. See Tab. 2 for the regional division. The layout force sensor is Pt_1 (horizontal direction: Y=0.2 m, vertical direction: Z=0.3 m) and Pt_2 (horizontal direction: Y=0 m, vertical direction: Z=0.2 m).

Table 2: Distribution of two bow segment parts

	Y [m]	Z [m]
Segment 1	-0.50<y<0.50	0.25<z<0.45
Segment 2	-0.50<y<0.50	0.00<z<0.25

6.1 Simulation of the rotational sliding of crushed ice in elastic boundary conditions

Fig. 17 displays the motion of the ice at different times during the structure-ice interaction. It can be observed that the ice contact with the structure rotates and slides along the structure surface. As the structure moves, the ice does not slide smoothly along the surface of the structure, and ice collides with the structure again during sliding. Ice that is not in contact with the structure also produces vertical motion.



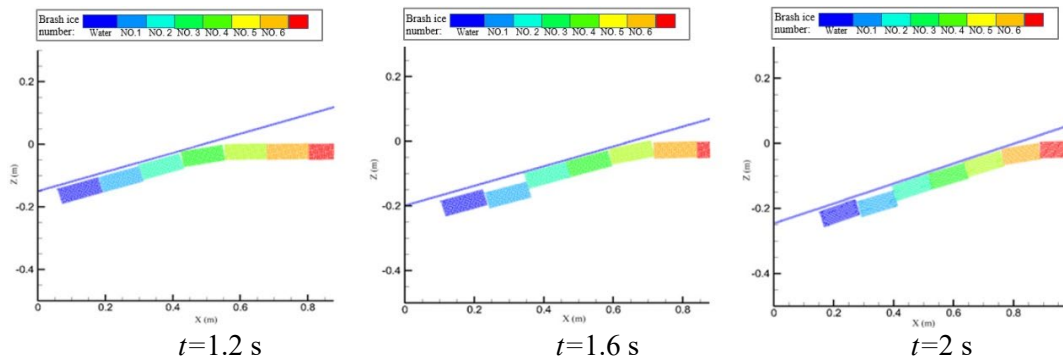


Figure 17: Motivation of ice rubble at different times

Fig. 18 displays the equivalent stress distribution in the crushed ice at different times during the structure-ice interaction, in which it can be observed from the figure that stress first appears in the contact area. When the ice rubble enters the water, the force is uniform. As the structure moves, the contact area between the different ice rubble components also exerts forces.

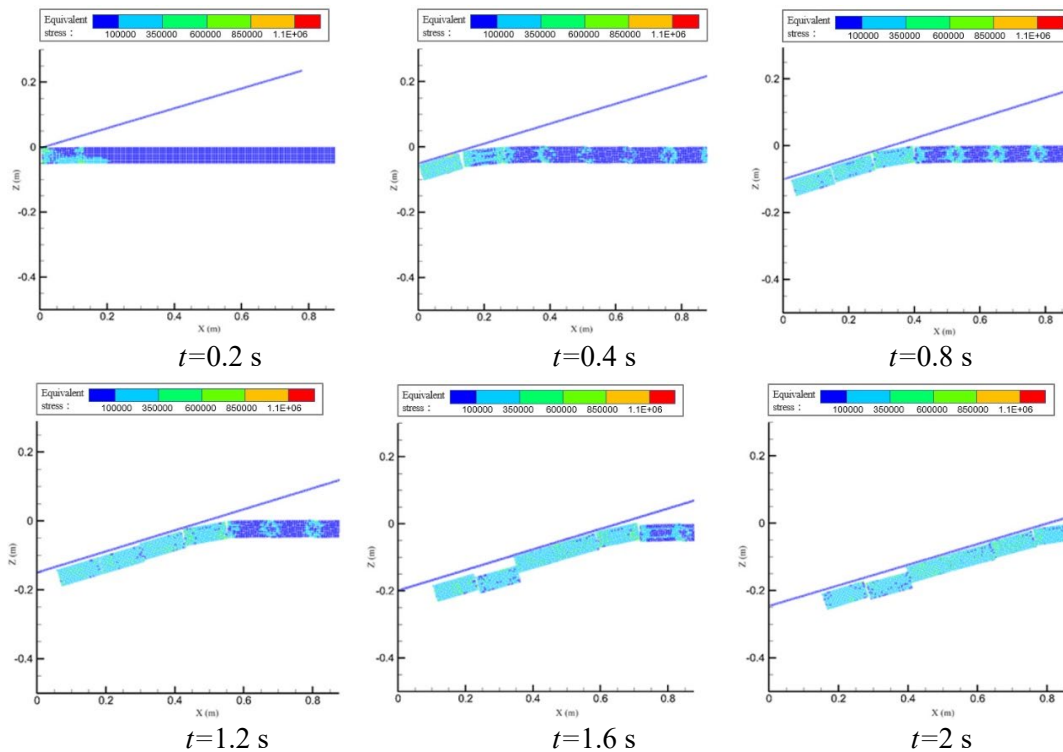


Figure 18: Contours of equivalent stress of ice in different times

Fig. 19 displays the results of ice resistance (immersion resistance) when the structure moves at a constant speed in the crushed ice with fluid (water) considered as the elastic

boundary support. It can be observed that the average ice resistance obtained using the CSPM is approximately 38.78 N, the test result is approximately 43.80 N, and the error is approximately 11.46%. It can be observed that when the ice sheet starts to collide with the structure, the ice resistance appears at an extreme value. When the crushed ice completes the rotary sliding process, it collides with the structure again. At this time, the ice resistance appears at an extreme value again. The structure pushes the ice forward, and the ice rubble components in the water hit the structure repeatedly, resulting in different peaks in the ice resistance. Further, the average force at Pt_1 obtained by CSPM is approximately 9.54 N, the test result is approximately 11.50 N, and the resulting error is approximately 17.04%. The average force at Pt_2 obtained by CSPM is approximately 6.23 N, the test result is approximately 7.58 N, and the error is approximately 17.81%. The ratio of the ice resistance of Segment 1 to Segment 2 is approximately 2.16, the ratio of test is approximately 1.83, and the error is approximately 18.03%, as indicated in Tab. 3.

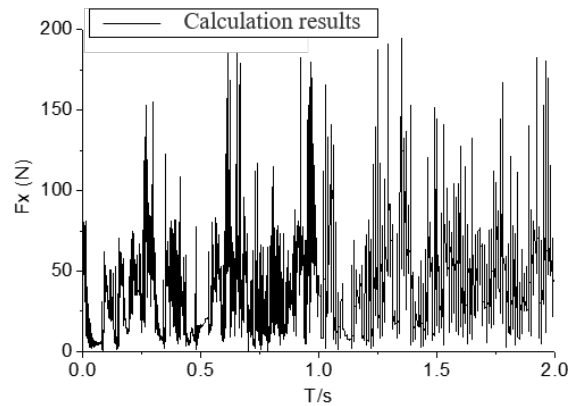


Figure 19: Ice-resistance versus time

Table 3: Ice resistance obtained by CSPM and experiment

	Test results	CSPM results	Error
Pt_1	11.505 N	9.54	17.14%
Pt_2	7.58 N	6.23	17.78%
Ratio of ice resistance in Segment 1 and Segment 2	1.83	2.16	18.20%
Immersion resistance	43.80 N	38.78	11.46%

6.2 Simulation of the rotational sliding of crushed ice in fluid-solid coupling

Fig. 20 displays the motion of the crushed ice at different times during the fluid-solid coupling. It can be observed that the ice rubble rotates individually and slides down the structure surface. With the movement of the structure, the ice influences the structure during the sliding process; however, the amplitude is clearly less than that in the elastic boundary condition. Water flows into the gap between the ice rubble components, and as it does, the ice rubble accelerates.

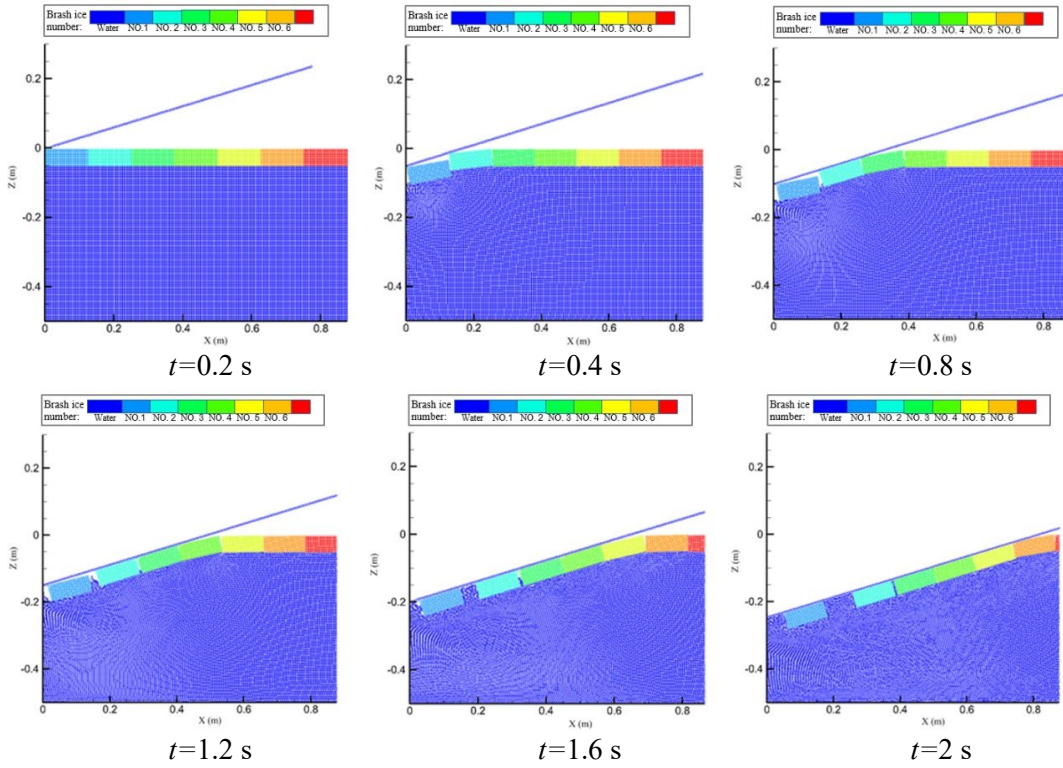
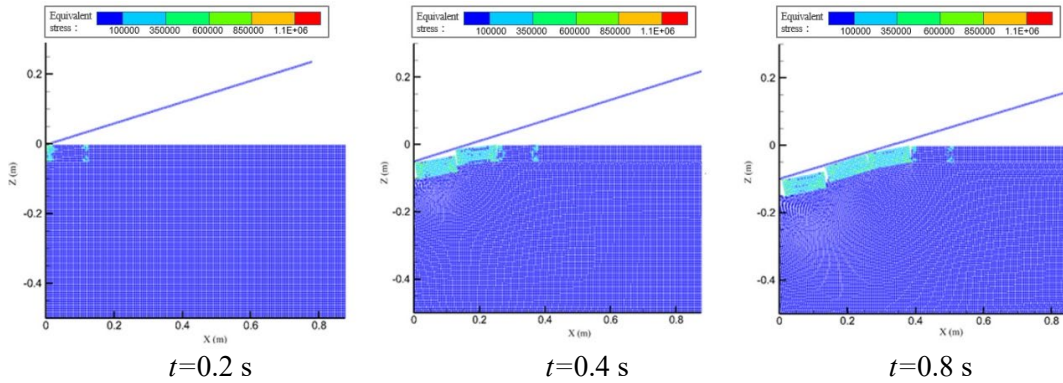


Figure 20: Contours of equivalent stress of ice floe at different times



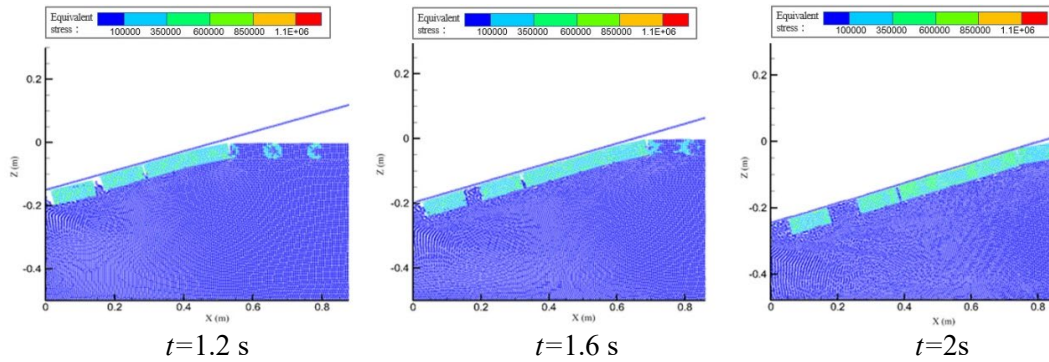


Figure 21: Contours of equivalent stress of ice in different times

Fig. 21 displays the equivalent stress distribution in the ice at different times during a 2 s icebreaking process. It can be observed that the stress first appears in the contact area, and then passes to a distant location; when the ice rubble enters the water, the force is relatively uniform. As the structure moves, force exists in the contact area between the different ice rubble components.

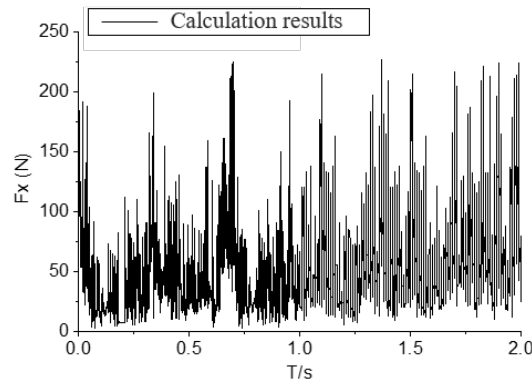


Figure 22: Ice-resistance versus time

Fig. 22 displays the CSPM calculation results of the ice resistance (immersion resistance) when the slope moves at a constant velocity of 0.4 m/s. It can be observed that the average ice resistance obtained by the CSPM method is approximately 47.15 N, the test result is approximately 43.8 N, and the error is approximately 7.65%. Combined with the movement of the ice rubble and the calculation results, it can be observed that when the ice starts to collide with the slope, a peak of ice resistance appears; when the ice rubble completes the rotational slip, it hits the slope again, and a peak ice resistance occurs. With the slope pushing forward, the ice rubble in the water repeatedly hits the slope, and the ice resistance produces different peaks. Further, the average force at Pt_1 obtained by the CSPM method is approximately 12.27 N, the test result is approximately 11.505 N, and the error is approximately 6.72%. The average force at Pt_2 obtained by the CSPM method is approximately 8.14 N, the test result is approximately 7.58 N, and the error is approximately 7.39%. The ratio of the ice resistance calculated by Segment 1 and

Segment 2 is approximately 1.81. The ratio of the test result is approximately 1.83 and the error is approximately 1.1%. as indicated in Tab. 4.

Table 4: Ice resistance obtained by CSPM and experiment

	Test results	CSPM results	Error
Pt 1	11.505 N	12.27	6.72%
Pt 2	7.58 N	8.14	7.39%
Ratio of ice resistance in Segment 1 and Segment 2	1.83	1.81	1.1%
Immersion resistance	43.80 N	47.15	7.65%

7 Conclusion

In this study, the improved CSPM method is combined with the material low-speed collision fracture model based on density correction and artificial stress correction to investigate the elastic boundary including the ventilation phenomenon and the fluid-solid coupling boundary of real fluid particles. Numerical simulation of the structure-ice-water interaction captured the characteristics in the continuous icebreaking process, i.e., the rotation and sliding of the ice fragments along the slope.

In both the boundary treatment modes of elastic boundary condition and fluid-solid coupling boundary condition, the icebreaking resistance performance and immersion resistance during icebreaking were investigated. The lengths of the crushed ice obtained by the two methods are close to the analytical solutions. The characteristics of force-time curve during the icebreaking process show a similar trend, but the latter gives more details. It is reasonable to treat the fluid as elastic support to reduce computational costs.

The improved CSPM method is used to simulate the immersion resistance test of Puntigliano [Puntigliano, Hamburgische Schiffbau-Versuchsanstalt GmbH (1995)]; the immersion resistance during the rolling and sliding process of the ice rubble is obtained and compared with the test results of Puntigliano. The ratio of the ice resistance calculated in Segment 1 and Segment 2 is approximately 1.8 for current loading condition. Further validation is needed for other loading conditions

Acknowledgment: This work is supported by the National Key Research and Development Program of China (2018YFC1406000, 2016YFE0202700) and the Central Fundamental Research Universities Special Fund (HEUCFM180110).

References

- Aksnes, V.** (2010): A simplified interaction model for moored ships in level ice. *Cold Regions Science and Technology*, vol. 63, no. 1-2, pp. 29-39.
- Benz, W.; Asphaug, E.** (1995): Simulations of brittle solids using smooth particle hydrodynamics. *Computer physics communications*, vol. 87, no. 1-2, pp. 253-265.
- Bui, H. H.; Fukagawa, R.; Sako, K.; Ohno, S.** (2008): Lagrangian meshfree particles method (SPH) for large deformation and failure flows of geomaterial using elastic-plastic

soil constitutive model. *International Journal for Numerical and Analytical Methods in Geomechanics*, vol. 32, no. 12, pp. 1537-1570.

Buzuev, A.; Rylvlin, A. Y. (1961): Calculation of the resistance encountered by an icebreaker moving through ice cakes and brash. *Morskoi Flot*, vol. 21, no. 8, pp. 136-138.

Chen, R. (2010): *An Improved MLSPH Method Theory Research and Application*. Hunan University (In Chinese).

Cho, S. R.; Jeong, S. Y.; Lee, S. (2013): Development of effective model test in pack ice conditions of square-type ice model basin. *Ocean Engineering*, vol. 67, pp. 35-44.

Deb, D.; Pramanik, R. (2013): Failure process of brittle rock using smoothed particle hydrodynamics. *Journal of Engineering Mechanics*, vol. 139, no. 11, pp. 1551-1565.

Eghtesad, A.; Shafiei, A. R.; Mahzoon, M. (2012): A new fluid-solid interface algorithm for simulating fluid structure problems in FGM plates. *Journal of Fluids and Structures*, vol. 30, pp. 141-158.

Gingold, R. A.; Monaghan, J. J. (1977): Smoothed particle hydrodynamics: theory and application to non-spherical stars. *Monthly Notices of the Royal Astronomical Society*, vol. 181, no. 3, pp. 375-389.

Hansen, E. H.; Løset, S. (1999): Modelling floating offshore units moored in broken ice: comparing simulations with ice tank tests. *Cold Regions Science and Technology*, vol. 29, no. 2, pp. 107-119.

He, Y.; Bayly, A. E.; Hassanpour, A. (2018): Coupling CFD-DEM with dynamic meshing: a new approach for fluid-structure interaction in particle-fluid flows. *Powder Technology*, vol. 325, pp. 620-631.

Jebaraj, C.; Swamidas, A. S. J.; Shih, L. Y. (1989): *Numerical Modelling of Ship/Ice Interaction*. National Research Council Canada, Institute for Marine Dynamics.

Jebaraj, C.; Swamidas, A. S. J.; Shih, L. Y.; Munaswamy, K. (1992): Finite element analysis of ship/ice interaction. *Computers & structures*, vol. 43, no. 2, pp. 205-221.

Karulin, E. B.; Karulina, M. M. (2011): Numerical and physical simulations of moored tanker behaviour. *Ships and Offshore Structures*, vol. 6, no. 3, pp. 179-184.

Kayo, Y. (1993): Measurement of ice load distribution on an icebreaker bow model composed by load panels. *Proceeding of the 12th POAC Conference*, vol. 1, pp. 328-337.

Keinonen, A.; Browne, R. P. (1991): Icebreaker performance prediction.

Khayyer, A.; Gotoh, H.; Falahaty, H.; Shimizu, Y. (2018): An enhanced ISPH-SPH coupled method for simulation of incompressible fluid-elastic structure interactions. *Computer Physics Communications*, vol. 232, pp. 139-164.

Kim, H. S.; Kim, M. C.; Choi, K. S.; Lee, C. J. (2013): Full scale ice sea trials of Korean ice breaking research vessel 'Araon' on the big floes near Antarctica. *Journal of Marine Science and Technology*, vol. 18, no. 4, pp. 515-523.

Kim, H. S.; Ryu, C. H.; Park, K. D.; Lee, J. (2014): Development of estimation system of ice resistance with surface information of hull form. *Ocean Engineering*, vol. 92, pp. 12-19.

Kim, M. C.; Lee, W. J.; Shin, Y. J. (2014): Comparative study on the resistance performance of an icebreaking cargo vessel according to the variation of waterline angles

in pack ice conditions. *International Journal of Naval Architecture and Ocean Engineering*, vol. 6, no. 4, pp. 876-893.

Konno, A.; Saitoh, O.; Watanabe, Y. (2011): Numerical investigation of effect of channel condition against ships resistance in brash ice channels. *Proceedings of the International Conference on Port and Ocean Engineering Under Arctic Conditions (No. POAC11-037)*.

Lau, M.; Lawrence, K. P.; Rothenburg, L. (2011): Discrete element analysis of ice loads on ships and structures. *Ships and Offshore Structures*, vol. 6, no. 3, pp. 211-221.

Li, S.; Liu, W. K. (2002): Meshfree and particle methods and their applications. *Applied Mechanics Reviews*, vol. 55, no. 1, pp. 1-34.

Libersky, L. D.; Petschek, A. G. (1991): Smooth particle hydrodynamics with strength of materials. *Advances in the Free-Lagrange Method Including Contributions on Adaptive Gridding and the Smooth Particle Hydrodynamics Method*, pp. 248-257.

Lindquist, A. (1989): Straightforward method for calculation of ice resistance of ships. *POAC'89*.

Liu, M. B.; Liu, G. R. (2010): Smoothed particle hydrodynamics (SPH): an overview and recent developments. *Archives of Computational Methods in Engineering*, vol 17, no. 1, pp. 25-76.

Liu, M. B.; Liu, G. R.; Lam, K. Y.; Zong, Z. (2003): Smoothed particle hydrodynamics for numerical simulation of underwater explosion. *Computational Mechanics*, vol. 30, no. 2, pp. 106-118.

Liu, G. R. (2016): An overview on meshfree methods: for computational solid mechanics. *International Journal of Computational Methods*, vol. 13, no. 5, 1630001.

Liu, R. W.; Xue, Y. Z.; Lu, X. K.; Cheng, W. X. (2018): Simulation of ship navigation in ice rubble based on peridynamics. *Ocean Engineering*, vol. 148, pp. 286-298.

Liukkonen, S.; Nortala-Hoikkanen, A. (1992): Ice resistance tests on a segmented icebreaker model. *IAHR Ice Symposium, Banff, Alberta*, pp. 296-308.

Lucy, L. B. (1977): A numerical approach to the testing of the fission hypothesis. *Astronomical Journal*, vol. 82, pp. 1013-1024.

Madenci, E.; Oterkus, E. (2014): Peridynamic theory. *Peridynamic Theory and Its Applications*, pp. 19-43.

Monaghan, J. J. (1994): Simulating free surface flows with SPH. *Journal of Computational Physics*, vol. 110, no. 2, pp. 399-406.

Müller, A.; Ettema, R. (1984): *Dynamic Response of an Ice-Breaker Hull to Ice Breaking (No. IIHR-273)*. IOWA INST of Hydraulic Research IOWA City.

Myland, D.; Ehlers, S. (2014): Theoretical investigation on ice resistance prediction methods for ships in level ice. *ASME 2014 33rd International Conference on Ocean, Offshore and Arctic Engineering*, vol. 10.

Peer, A.; Gissler, C.; Band, S.; Teschner, M. (2018): An implicit SPH formulation for incompressible linearly elastic solids. *Computer Graphics Forum*, vol. 37, no. 6, pp. 135-148.

Puntigliano, F. (1995): *On the Resistance Components Below the Waterline in the Continuous Mode of Icebreaking: Model Tests*. Hamburgische Schiffbau-Versuchsanstalt GmbH, Hamburg (Germany).

Randles, P. W.; Libersky, L. D. (1996): Smoothed particle hydrodynamics: some recent improvements and applications. *Computer Methods in Applied Mechanics and Engineering*, vol. 139, no. 1-4, pp. 375-408.

Riska, K. (1997): *Performance of Merchant Vessels in Ice in the Baltic*. Sjöfartsverket.

Sawamura, J. (2012): Numerical investigation of ice bending failure and ice submerging force for ship maneuvering in level ice. *Proceeding 21st International Symposium on Ice*.

Shi, Y.; Li, S.; Chen, H.; He, M.; Shao, S. (2018): Improved SPH simulation of spilled oil contained by flexible floating boom under wave-current coupling condition. *Journal of Fluids and Structures*, vol. 76, pp. 272-300.

Valanto, P.; Jones, S. J.; Enkvist, E.; Izumiyama, K. (2001): The resistance of ships in level ice. discussion. Author's closure. *Transactions-Society of Naval Architects and Marine Engineers*, vol. 109, pp. 53-83.

Valanto, P. U. (1989): *Experimental and Theoretical Investigation of the Icebreaking Cycle in Two Dimensions*. University of California, Berkeley.

Yamaguchi, H.; Suzuki, Y.; Uemura, O.; Kato, H.; Izumiyama, K. (1997): Influence of bow shape on icebreaking resistance in low speed range. *Proceedings of the International Conference on Offshore Mechanics and Arctic Engineering*, pp. 51-62.

Zhang, N.; Zheng, X.; Ma, Q. (2017): Updated smoothed particle hydrodynamics for simulating bending and compression failure progress of ice. *Water*, vol. 9, no. 11, pp. 882.

Zheng, X.; Ma, Q. W.; Duan, W. Y. (2014): Incompressible SPH method based on Rankine source solution for violent water wave simulation. *Journal of Computational Physics*, vol. 276, pp. 291-314.

Zheng, X.; Shao, S.; Khayyer, A.; Duan, W.; Ma, Q. et al. (2017): Corrected first-order derivative ISPH in water wave simulations. *Coastal Engineering Journal*, vol. 59, no. 1, 1750010.